





Kinetic simulations of solar wind plasma irregularities crossing the Hermean magnetopause

G. Voitcu¹ , M. Echim^{1,2,3} , E. Teodorescu¹ , and C. Munteanu¹ 

¹ Institute of Space Science, Măgurele 077125, Romania
e-mail: gabi@spacescience.ro

² Royal Belgian Institute for Space Aeronomy, Brussels 1180, Belgium

³ Belgian Solar Terrestrial Center of Excellence, Brussels, Belgium

Received 22 February 2023 / Accepted 20 April 2023

ABSTRACT

Context. The physical mechanisms that favor the access of solar wind plasma into the magnetosphere have not been entirely elucidated to date. Studying the transport of finite-sized magnetosheath plasma irregularities across the magnetopause is fundamentally important for characterizing the Hermean environment (of Mercury) as well as for other planetary magnetic and plasma environments.

Aims. We investigate the kinetic effects and their role on the penetration and transport of localized solar wind or magnetosheath plasma irregularities within the Hermean magnetosphere under the northward orientation of the interplanetary magnetic field.

Methods. We used three-dimensional (3D) particle-in-cell (PIC) simulations adapted to the interaction between plasma elements (irregularities or jets) of a finite spatial extent and the typical magnetic field of Mercury's magnetosphere.

Results. Our simulations reveal the transport of solar wind plasma across the Hermean magnetopause and entry inside the magnetosphere. The 3D plasma elements are braked and deflected in the equatorial plane. The entry process is controlled by the magnetic field gradient at the magnetopause. For reduced jumps of the magnetic field (i.e., for larger values of the interplanetary magnetic field), the magnetospheric penetration is enhanced. The equatorial dynamics of the plasma element is characterized by a dawn-dusk asymmetry generated by first-order guiding center drift effects. More plasma penetrates into the dusk flank and advances deeper inside the magnetosphere than in the dawn flank.

Conclusions. The simulated solar wind or magnetosheath plasma jets can cross the Hermean magnetopause and enter into the magnetosphere, as described by the impulsive penetration mechanism.

Key words. plasmas – magnetic fields – planet–star interactions – methods: numerical

1. Introduction

The Earth's magnetopause is frequently impacted by finite-sized plasma irregularities of solar wind or magnetosheath origins that generate various effects on the geomagnetic environment (e.g., [Lemaire & Roth 1978](#); [Plaschke et al. 2016](#)). These plasma irregularities are known in the scientific literature under various names, for instance, as filamentary plasma elements ([Lemaire 1977](#); [Lundin & Aparicio 1982](#); [Lyatsky et al. 2016a](#)), plasmoids ([Lemaire 1985](#); [Echim & Lemaire 2000](#); [Gunell et al. 2014](#); [Karlsson et al. 2015](#); [Goncharov et al. 2020](#)), transient flux enhancements ([Němeček et al. 1998](#)), high-kinetic energy density jets ([Amata et al. 2011](#)), super-fast plasma streams ([Savin et al. 2012](#)), localized density enhancements ([Karlsson et al. 2012](#)), dynamic pressure enhancements ([Archer & Horbury 2013](#)), or high-speed magnetosheath jets ([Plaschke et al. 2013](#); [Wing et al. 2014](#); [Vuorinen et al. 2019](#); [Escoubet et al. 2020](#); [Raptis et al. 2020](#); [Dmitriev et al. 2021](#)). Some of them are able to penetrate the magnetopause and have been observed deep inside the magnetosphere ([Lundin & Aparicio 1982](#); [Lundin et al. 2003](#); [Gunell et al. 2012](#); [Shi et al. 2013](#); [Dmitriev & Suvorova 2015](#); [Lyatsky et al. 2016a,b](#)). For instance, [Lundin et al. \(2003\)](#) and [Gunell et al. \(2012\)](#) used Cluster data to study the penetration of solar wind plasma clouds and magnetosheath plasmoids through the dayside magnetopause. These authors conclude that the transport process inside the magnetosphere exhibit similarities

with the impulsive penetration mechanism proposed by [Lemaire & Roth \(1978\)](#) to explain such phenomena. [Dmitriev & Suvorova \(2015\)](#) performed a statistical analysis of the jets detected by THEMIS in the magnetosheath and showed that more than 60% of them do penetrate across the magnetopause and do have, overall, electrodynamic properties consistent with the impulsive penetration mechanism. The investigations of [Lyatsky et al. \(2016a,b\)](#) based on Cluster observations emphasize the stable antisunward motion of the magnetosheath filaments inside the magnetosphere, suggesting their detachment from the magnetosheath background and penetration inside the magnetosphere.

The transport of finite-sized plasma irregularities across magnetic discontinuities, as the magnetopause, is a key process not only for the geomagnetic environment, but also for other planetary plasma environments. Recently, [Karlsson et al. \(2016, 2021\)](#) used MESSENGER data to study the small-scale plasma structures in Mercury's magnetosheath. Their investigation revealed a relatively large number of localized magnetic structures in the Hermean magnetosheath (of Mercury) and nearby solar wind with similar properties to the high-speed plasma jets identified in the Earth's magnetosheath. Unfortunately, due to some limitations in the plasma measurements on board MESSENGER, this study does not provide the density and bulk velocity of the observed structures, but only their magnetic signatures. The BepiColombo mission around Mercury will provide a great opportunity to continue this kind of investigation.

The interaction of localized plasma structures with non-uniform magnetic fields was simulated in the past using both fluid and kinetic approaches. There are several magnetohydrodynamic and hybrid simulations performed in a magnetospheric context as, for instance, [Ma et al. \(1991\)](#), [Savoini et al. \(1994\)](#), [Dai & Woodward \(1994, 1995, 1998\)](#), [Huba \(1996\)](#). The physics treated by these simulations is truncated since important physical processes occurring at kinetic scales, such as the self-polarization electric field, are disregarded (see [Echim & Lemaire 2000](#) for a review). More recently, [Palmroth et al. \(2018, 2021\)](#) used two-dimensional (2D) hybrid-Vlasov simulations to investigate the formation and properties of high-speed plasma jets in the Earth's magnetosheath. It has been shown that the simulated jets exhibit similar features with the ones detected in-situ in the magnetosheath. Similarly, [Preisser et al. \(2020\)](#) proposed various generation mechanisms of localized jets or plasmoids based on 2D hybrid simulations. All the cited papers are focused on jets formation or properties and did not discuss their interaction with the magnetopause and the subsequent evolution. In the Hermean environment, [Fatemi et al. \(2020\)](#) used the AMITIS code ([Fatemi et al. 2017](#)) to run three-dimensional (3D) hybrid simulations for the precipitation of solar wind protons onto the surface of planet Mercury under various solar wind conditions, but did not consider the problem of plasma jets.

The fully kinetic simulations performed on the topic of finite-sized plasma irregularities interaction with magnetic barriers (e.g., [Galvez 1987](#); [Galvez et al. 1988](#); [Livesey & Pritchett 1989](#); [Galvez & Borovsky 1991](#); [Cai & Buneman 1992](#); [Neubert et al. 1992](#); [Hurtig et al. 2003](#); [Gunell et al. 2009](#)) are limited to magnetic configurations that are either uniform or very specific for certain laboratory experiments, thus only partially relevant for the interaction of high-speed plasma jets with planetary magnetospheres. [Karimabadi et al. \(2014\)](#) considered 2D fully kinetic and hybrid approaches to simulate the solar wind interaction with the terrestrial magnetosphere. It has been argued that the foreshock turbulence gives rise to high-speed plasma jets that further move inside the magnetosheath. Some of the simulated jets reach the magnetopause, but are not traced further.

[Voitcu & Echim \(2016, 2017\)](#) used 3D particle-in-cell (PIC) simulations to emphasize the electric self-polarization of finite-sized plasma irregularities or jets streaming across transverse magnetic discontinuities. It has been shown that the plasma-field interaction process is controlled by the height of the magnetic barrier and the initial momentum of the plasma jets, separating them into penetrating and non-penetrating ones. While the penetrating jets are braked when the magnetic field increases, the non-penetrating ones are split into two counter-streaming flows drifting tangentially to the magnetic discontinuity surface. Their kinetic structure revealed the presence of crescent-shaped velocity distributions after the interaction with the magnetic discontinuity ([Voitcu & Echim 2018](#)). More recently, [Lavorenti et al. \(2022\)](#) considered an implicit particle-in-cell code (iPIC3D – [Markidis et al. 2010](#)) to globally simulate the magnetosphere of planet Mercury. These authors focused on the self-consistent formation and characterization of the magnetosphere under different orientations of the interplanetary magnetic field (IMF), but did not envisage the problem of high-speed plasma jets interacting with the magnetopause.

In this paper, we used 3D PIC simulations and theoretical modeling to study the kinetic effects associated with the interaction between finite-sized solar wind or magnetosheath plasma structures and the dayside region of the Hermean magnetosphere under a northward orientation of the interplanetary magnetic field. We focus on the equatorial dynamics and asymmetric

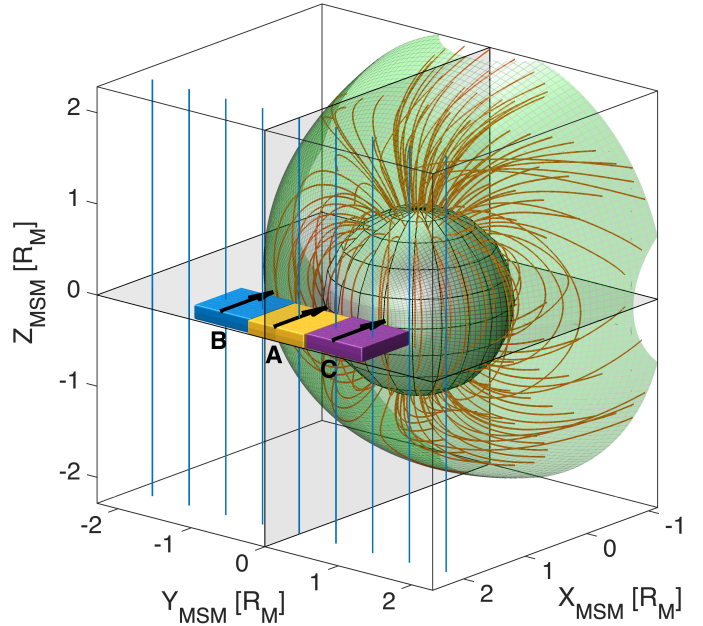


Fig. 1. Simulation setup for cases A (frontal injection), B (dawn flank injection), and C (dusk flank injection) in the MSM reference frame. The Hermean magnetopause is drawn in green according to Shue's model ([Shue et al. 1997](#)). The KT17 magnetic field lines ([Korth et al. 2017](#)) are represented in red, while the northward magnetic field lines outside Mercury's magnetosphere are shown in blue. We illustrate with colored boxes the injection regions corresponding to the three simulated plasma structures: Yellow for case A, blue for case B, and purple for case C. The initial plasma bulk velocity is shown with black arrows.

evolution of the plasma structures penetrating inside the magnetospheric cavity. Thus, we extend our previous PIC simulations on the topic of plasma-field interaction near magnetic discontinuities ([Voitcu & Echim 2016, 2017, 2018](#)) by considering a simulation setup which corresponds to the magnetosphere of planet Mercury. While the aforementioned simulations were “local,” here we discuss a more “global” approach that is specific to a small magnetospheric system. We provide new physical insight on the transport mechanisms of penetrating plasma inside the Hermean magnetosphere. The simulation results are discussed in the context of the impulsive penetration mechanism ([Lemaire 1985](#)).

This paper is organized as follows. In the second section, we describe the setup of our simulations. In the third section, we present the results obtained, while in the last section, we give our conclusions.

2. Simulation setup

The simulation setup illustrated in [Fig. 1](#) is adapted for the interaction between 3D plasma structures originating from the solar wind or magnetosheath and the dayside magnetosphere of planet Mercury. Since our goal is to investigate the local microphysics of the interaction process in the vicinity of the Hermean magnetopause, we assume that the global magnetospheric configuration is established prior to the interaction of the finite-sized plasma structures with the magnetosphere. Thus, the global simulation of the Hermean magnetosphere formation is beyond the scope of our paper. The simulated magnetic field has two components, namely, (i) the background (or external) magnetic field and (ii) the internal magnetic field produced by the localized plasma

element itself. The background magnetic field is steady-state and is added at each time-step to the self-consistent field computed during the simulation runtime. It also has two components corresponding to (i) the magnetospheric field of Mercury and (ii) the solar wind. The transition between these two components of the magnetic field is imposed along a 3D surface defined by Shue's model of the magnetopause (Shue et al. 1997). Thus, for a given position (x, y, z) within the simulation domain, the background magnetic field is:

$$\mathbf{B}_{\text{BG}}(x, y, z) = \begin{cases} \mathbf{B}_{\text{MSP}}(x, y, z) & \text{for } r(x, y, z) < r_{\text{MP}} \\ \mathbf{B}_{\text{IMF}} = \mathbf{B}_0 & \text{for } r(x, y, z) \geq r_{\text{MP}} \end{cases}, \quad (1)$$

where: \mathbf{B}_{MSP} is the magnetospheric field of planet Mercury provided by the KT17 model (Korth et al. 2017), \mathbf{B}_{IMF} is the interplanetary magnetic field which is assumed to be uniform, r is the radial distance from Mercury's dipole to the (x, y, z) point, and r_{MP} is the radial distance to the 3D magnetopause surface.

The background plasma is disregarded in the present work and the finite-sized plasma element is streaming in a vacuum towards the magnetopause, similarly to a high-speed plasma jet characterized by an excess of dynamic pressure in a tenuous background environment (e.g., Karlsson et al. 2012). The presence of a background plasma directly impacts the parallel and perpendicular dynamics of the high-speed plasma jets, as discussed, for instance, by Borovsky (1987). The laboratory experiments performed by Wessel et al. (1988) have shown that the background plasma can reduce the self-polarization electric field and cross-field propagation, but only for background densities equal to or larger than the plasmoid density. Thus, for high-speed plasma jets characterized by an excess of density with respect to the background plasma, as the ones observed in the magnetosheath, the cross-field propagation is possible. We plan to include a background plasma in our future simulations.

The electrons and protons of the finite-sized plasma element are uniformly distributed over a 3D region outside the magnetosphere at $t = 0$. The injection area is localized close to the subsolar magnetopause in case A (frontal injection) and in the two magnetospheric flanks in cases B (dawn flank injection) and C (dusk flank injection). Their initial velocities are generated according to a displaced Maxwellian with the average velocity pointing along the negative X_{MSM} direction, where MSM denotes the Mercury solar magnetospheric coordinate system. The two species have identical densities and temperatures at $t = 0$. The IMF direction is northward, while the initial self-consistent electric and magnetic fields are set to 0 in the entire simulation domain. There is no external electric field.

The plasma-beta parameter is small ($\beta = 0.01$) and the plasma dielectric constant is large ($\varepsilon = 190$); $\varepsilon = 1 + (\omega_{pi}/\omega_{Li})^2$, where ω_{pi} and ω_{Li} are the ion Langmuir and Larmor frequencies (e.g., Chen 1984). For large values of ε , the self-polarization electric field plays an important role for the propagation of the plasma element across the magnetic field (e.g., Schmidt 1960; Lemaire 1985; Echim & Lemaire 2005; Voitcu & Echim 2016). The perpendicular size of the plasma element with respect to the IMF direction, L_{\perp} , is 13 times larger than the thermal ion Larmor radius, that is, equal to 0.76 Mercury radii. These values are consistent with the scale sizes determined by Karlsson et al. (2021) for the localized magnetic structures identified by MESSENGER in Mercury's magnetosheath and the nearby solar wind. Thus, we simulate small Larmor radius plasma clouds that are large with respect to the Hermean magnetospheric cavity.

Table 1. Input parameters

Parameter	All cases
m_i/m_e	36
U_0/V_{Te}	0.36
U_0/V_{Ti}	2.17
β	0.01
ε	190
L_{\perp}/r_{Li}	13
L_{\perp}/R_{M}	0.76
IMF direction	northward
B_{ss}/B_0	1.81
$m_x \times m_y \times m_z$	$405 \times 255 \times 605$
np	20 000 000
N_c	100

Notes. m_i/m_e – ion-to-electron mass ratio, U_0 – plasma bulk velocity at injection, V_{Te} and V_{Ti} – thermal speed of electrons and ions, β – plasma-beta, ε – plasma dielectric constant, L_{\perp} – transversal size of the plasma element (with respect to the IMF direction), r_{Li} – Larmor radius of thermal ions, R_{M} – radius of Mercury, B_{ss} – magnetic field magnitude at the subsolar magnetopause (just inside the magnetosphere), B_0 – IMF magnitude, m_x, m_y, m_z – number of simulation grid-cells along each direction, np – total number of simulated particles per species, and N_c – number of particles per grid-cell per species.

Our simulation code embraces a similar approach to the one employed by Buneman (1993) in TRISTAN. The PIC model is explicit, electromagnetic, and relativistic. The geometry is 3D in the configuration space and velocity space. The boundaries of the simulation domain are periodic and kept as far as possible from the localized plasma element. Currently, there are no inner boundary conditions for the planetary surface. To quantify the amount of plasma crossing Mercury's surface at a given time, we define the planetary penetration degree: $\Gamma_{\text{P}}(t) = M_{\text{IN}}(t)/M_0$, where M_{IN} is the total mass of plasma reaching the surface of Mercury at a time, t , while M_0 is the initial mass of the plasma element. Since the charged particles are injected from the solar wind, $\Gamma_{\text{P}}(0) = 0$. In order to avoid the unrealistic accumulation of plasma inside the planet, the simulation is stopped when the planetary penetration degree reaches a certain critical threshold, namely, $\Gamma_{\text{P}} = 4\%$.

The list of input parameters used in cases A, B, and C is given in Table 1. The center of the plasma element at $t = 0$ is localized in (X_0, Y_0, Z_0) in the MSM reference system. All three plasma elements are injected from the equatorial plane, that is, $Z_0 = 0$. In case A, $Y_0 = 0$ (frontal injection), while in cases B and C, $Y_0 = \mp 0.76 R_{\text{M}}$ (injection from flanks). The total number of simulated particles is 20 million per species, while the number of particles per simulation grid-cell at initialization is 100 per species. The proton-to-electron mass ratio is 36. For the KT17 model, we used the following input parameters: $r_{\text{h}} = 0.39$ AU and $\text{DI} = 50$, where r_{h} is Mercury's heliocentric distance expressed in astronomical units and DI the magnetic disturbance index (Anderson et al. 2013). The subsolar magnetopause distance used in Shue's model is $R_{\text{ss}} = (2.06873 - 0.00279 \cdot \text{DI}) \cdot r_{\text{h}}^{1/3}$ (Korth et al. 2017), while the magnetotail flaring level is $\alpha = 0.5$.

The physical quantities are normalized as follows throughout the paper: the number density to the initial value, n_0 , the charge

density to $\rho_0 = en_0$ (where e is the elementary charge), the bulk velocity to the injection value, U_0 , the magnetic field induction to the IMF value, B_0 , the electric field intensity to $E_0 = U_0 B_0$ and the spatial coordinates to Mercury's radius, R_M .

3. Numerical results

In the first simulated case, the plasma element is injected upstream the subsolar magnetopause: $\Delta R = 2.6 r_{Li} = 0.15 R_M$, where ΔR is the distance between the propagation front of the plasma element at $t = 0$ and the magnetopause nose located at $R_{ss} = 1.41 R_M$. The background magnetic field increases by 81% across the model magnetopause, from B_0 in the solar wind and magnetosheath to B_{ss} just inside the magnetosphere. The simulation is stopped at $\omega_{Li} t = 10$ when $\Gamma_P = 4\%$; ω_{Li} is the ion Larmor frequency outside the magnetosphere. The plasma bulk velocity is computed from the average velocities of the electrons and ions: $\mathbf{U} = (\rho_{me} \mathbf{U}_e + \rho_{mi} \mathbf{U}_i) / (\rho_{me} + \rho_{mi})$, where ρ_{me} and ρ_{mi} are the mass densities of the two plasma species. Note: the bulk velocity is calculated only for those grid-cells with particle densities higher than 8% of n_0 in order to avoid unrealistically large velocities in the less populated bins. This high-density core of the plasma element is illustrated with a white or blue contour in various plots throughout the paper.

The key element that sustains the transport of finite-sized plasma structures across magnetic barriers, such as the magnetopause, is the self-polarization electric field (e.g., Schmidt 1960; Borovsky 1987). When a plasma element of finite spatial extent is injected into a transverse magnetic field, the charge-dependent Lorentz force deflects the electrons and ions in opposite directions and two space charge layers of reversed polarity are formed at its lateral edges across the perpendicular direction to both the magnetic field and plasma bulk velocity. As long as $\varepsilon \gg 1$, these layers maintain a polarization electric field inside the quasineutral bulk of plasma that further sustains its cross-field propagation: $\mathbf{E}_0 = \mathbf{B}_0 \times \mathbf{U}_0$.

In Fig. 2, we illustrate the self-polarization kinetic effect for case A, shortly after injection ($\omega_{Li} t = 0.6$) and prior to the interaction with the non-uniform magnetic field. The top and middle panels show the total charge density ($\rho = \rho_e + \rho_i$) and self-consistent electric field in the $X_{MSM} = 1.96 R_M$ cross-section localized outside the magnetosphere. The electric field is drawn with vectors and its E_y component is color-coded. Large purple arrows are used to indicate the background magnetic field orientation. The bottom panel illustrates the variation profiles of $\rho(y)$ and $E_y(y)$ averaged along the magnetic field direction from $Z_{MSM} = -0.11 R_M$ to $Z_{MSM} = +0.11 R_M$. This interval corresponds to the bulk region of plasma bounded by the white contour in the top and middle panels. The horizontal yellow line marks the value of $E_y = -E_0$. We can easily notice that the lateral edges of the plasma element are electrically polarized. Indeed, a negative space charge layer is observed around $Y_{MSM} \approx -0.37 R_M$, while a positive one is evidenced around $Y_{MSM} \approx +0.40 R_M$. They are illustrated with tall magenta boxes in Fig. 2. In the region between these two layers, the plasma is quasineutral ($\rho \approx 0$) and the electric field intensity is $E_y \approx -U_0 B_0$. This self-polarization electric field drives the plasma element across the transverse magnetic field.

In the top panel of Fig. 3, we illustrate the electron number density at the end of run, while in the middle panel, the U_x component of the plasma bulk velocity, both for the meridional cross-section $Y_{MSM} = 0$. The plasma element injected from the solar wind is able to penetrate inside the Hermean magnetosphere. Indeed, as can be noticed in Fig. 3, almost

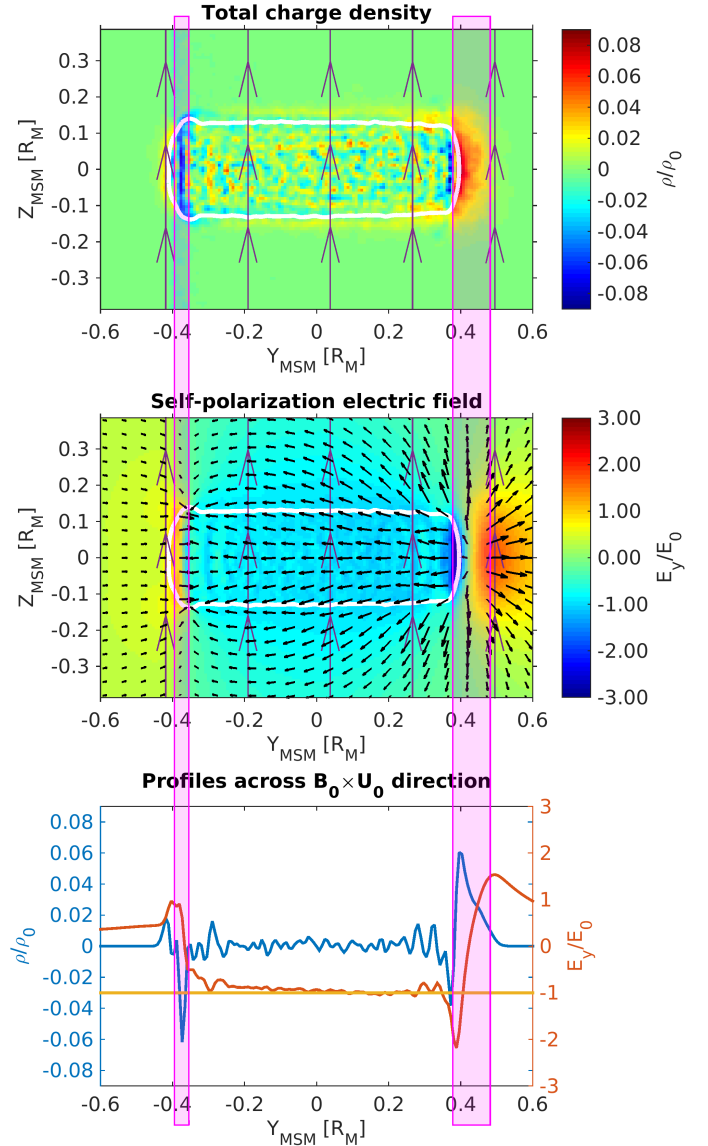


Fig. 2. Self-polarization of the plasma element shortly after injection ($\omega_{Li} t = 0.6$, where ω_{Li} is the ion Larmor frequency outside the magnetosphere) in the $X_{MSM} = 1.96 R_M$ cross-section inside the simulation domain for case A: (top) total charge density and (middle) self-consistent electric field illustrated with vectors (the E_y component is color coded). The profiles of the charge density (blue) and E_y electric field (red) across Y_{MSM} (bottom). These profiles are averaged along the Z_{MSM} direction parallel to the magnetic field (shown with large purple arrows in the top and middle panels) from $-0.11 R_M$ to $+0.11 R_M$. The white contour in the top and middle panels encloses the high-density core of the plasma element, while the yellow horizontal line in the bottom panel is drawn at $E_y = -U_0 B_0$. The tall magenta boxes mark the two space charge layers of opposite polarity formed at the edges of the plasma element.

the entire plasma structure is located downstream the Shue's magnetopause at the end of run. The magnetospheric entry is accompanied by the strong braking of the plasma element while streaming into the increasingly larger magnetic field. The bulk velocity is reduced from U_0 , prior to the interaction with the magnetopause, to $U_x \approx 0$, at the propagation front in $Z_{MSM} = 0$. Simultaneously, the penetrating plasma is expanding along the magnetic field lines towards the planetary surface at high

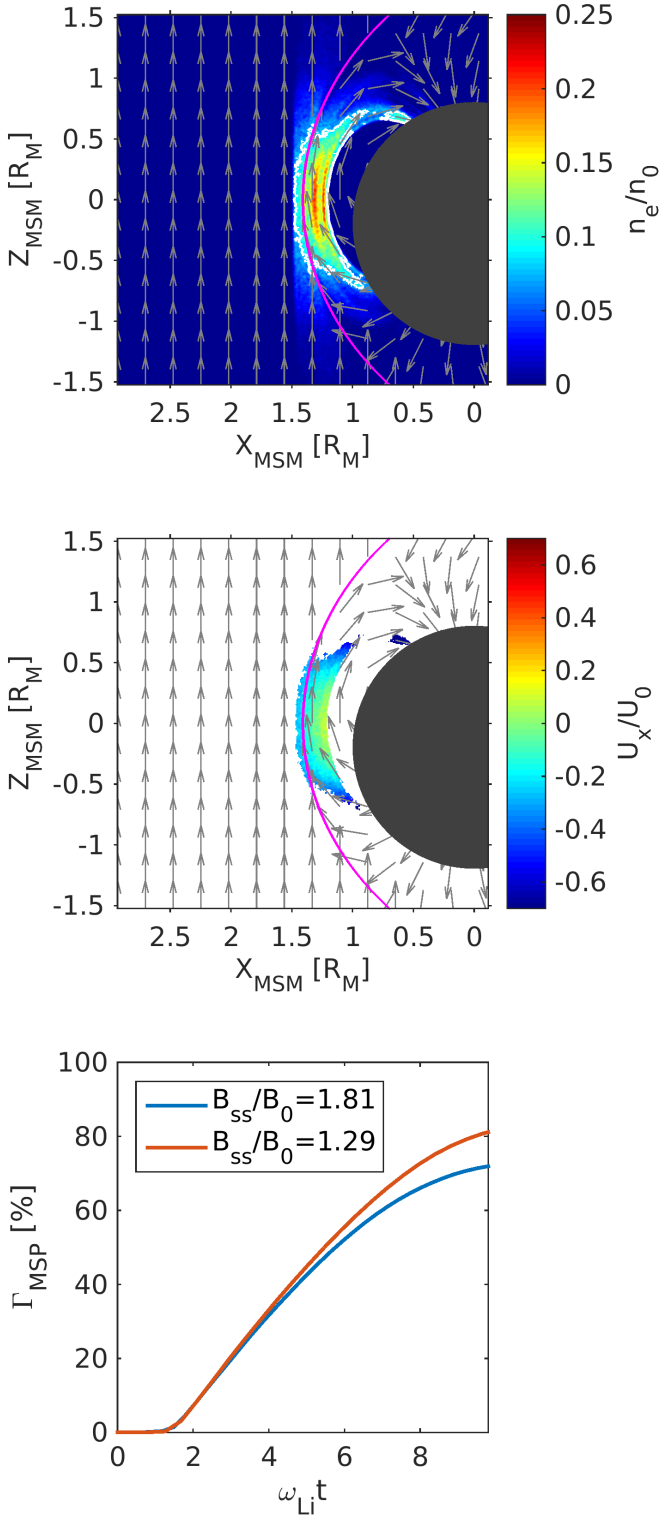


Fig. 3. Cross-section $Y_{\text{MSM}} = 0$ inside the simulation domain for case A: (top) electron number density and (middle) plasma bulk velocity along the X_{MSM} axis at the end of run ($\omega_{\text{Li}}t = 10$), where ω_{Li} is the ion Larmor frequency outside the magnetosphere. Both quantities are normalized to their corresponding initial values. The magenta curve illustrates the magnetopause, while the grey arrows indicate the background magnetic field unit vectors. Note: the small overlap of magnetic field vectors in different regions of the simulation domain is just an artifact. The magnetospheric penetration degree variation from initialization to the end of run for $B_{\text{ss}}/B_0 = 1.81$ is shown at bottom (blue curve) and $B_{\text{ss}}/B_0 = 1.29$ (red curve), where B_{ss} is the magnetic field at the sub-solar magnetopause just inside the magnetosphere and B_0 the magnetic field outside the magnetosphere.

latitudes. The electron density in the top panel of Fig. 3 is characterized by wave structures that can also be observed in later figures. Wave phenomena in plasmoids penetrating across magnetic barriers have been emphasized in the past with numerical simulations (e.g., Gunell et al. 2008, 2009), satellite measurements (e.g., Gunell et al. 2014) and laboratory experiments (e.g., Hurtig et al. 2004). The study of waves is beyond the scope of our paper, but we shall approach these phenomena in a future publication.

In order to quantify the entry process, we defined the magnetospheric penetration degree: $\Gamma_{\text{MSP}}(t) = M_{\text{IN}}^*(t)/M_0$, where M_{IN}^* is the total mass of plasma penetrating inside the magnetosphere at time t (i.e., downstream the magnetopause). Since the charged particles are injected from the solar wind, $\Gamma_{\text{MSP}}(0) = 0$. The blue curve in the bottom panel of Fig. 3 shows the time evolution of Γ_{MSP} for case A. By the end of run, 72% of the initial mass of plasma injected from the solar wind crossed the magnetopause surface and entered inside the magnetosphere. This ratio is higher when the magnetic jump at the magnetopause is reduced. Indeed, by running a supplemental simulation with $B_{\text{ss}}/B_0 = 1.29$, we obtained a magnetospheric penetration degree of 81% at $\omega_{\text{Li}}t = 10$ (the red curve in Fig. 3). We note that the plasma dielectric constant was kept unchanged in the new simulation run in order to maintain the same level of electric self-polarization. Thus, by reducing the height of the magnetic barrier, $B_{\text{ss}} - B_0$, by 50%, the amount of plasma crossing the magnetopause increases by $(M_{\text{IN}}^{*2} - M_{\text{IN}}^{*1})/M_{\text{IN}}^{*1} = 13\%$, where an upper index of 1 refers to $B_{\text{ss}}/B_0 = 1.81$ and an upper index of 2 to $B_{\text{ss}}/B_0 = 1.29$.

The dynamics of the plasma element in the equatorial plane ($Z_{\text{MSM}} = 0$) is emphasized in Fig. 4, where we illustrate the electron and ion densities (top panels), perpendicular bulk velocity components (middle panels), and perpendicular electric field components (bottom panels) at the end of run ($\omega_{\text{Li}}t = 10$). We note that the plasma element is deflected along both the positive and negative directions of the Y_{MSM} axis as it enters inside the magnetosphere. Indeed, $U_y > 0$ for the plasma regions having $Y_{\text{MSM}} > 0$ and, oppositely, $U_y < 0$ for $Y_{\text{MSM}} < 0$. At the furthest areas of the plasma element along Y_{MSM} , we have $|U_y| \approx U_0/2$. This deflection process is sustained by the E_x component of the electric field which is negative for $Y_{\text{MSM}} > 0$ and positive for $Y_{\text{MSM}} < 0$. On the other hand, $U_x < 0$ for $Y_{\text{MSM}} > 0$ and $U_x \approx 0$ for $Y_{\text{MSM}} < 0$, consistent with the sign of E_y . Thus, the duskward wing of the deflected plasma element is streaming faster along $-X_{\text{MSM}}$ with respect to the downward wing which is virtually stopped, leading to an asymmetric evolution inside the magnetosphere.

To better visualize the equatorial dynamics of the penetrating plasma element, the orientation and magnitude of the perpendicular plasma bulk velocity are shown in the top panels of Fig. 5. In the bottom panels, we plot the orientation and magnitude of the zero-order (or electric) drift velocity, $\mathbf{U}_E = \mathbf{E} \times \mathbf{B}/B^2$, computed with the self-consistent electric field (illustrated in the bottom panels of Fig. 4) and the background magnetic field illustrated with the greenish color map (since $\beta \ll 1$, we neglected the self-consistent magnetic field). By comparing the top and bottom panels of Fig. 5, we can notice that the penetrating plasma is drifting with $U_{\perp} \approx U_E$ inside the magnetosphere and the Y_{MSM} deflection is not totally symmetrical. The perpendicular bulk velocity is a bit larger in the dusk flank ($Y_{\text{MSM}} > 0$) than in the dawn flank ($Y_{\text{MSM}} < 0$). This dawn-dusk asymmetry in the equatorial plane can be observed also in the top panels of Fig. 4. Indeed, the particle density is larger in the dusk flank with respect to the dawn flank for both plasma species.

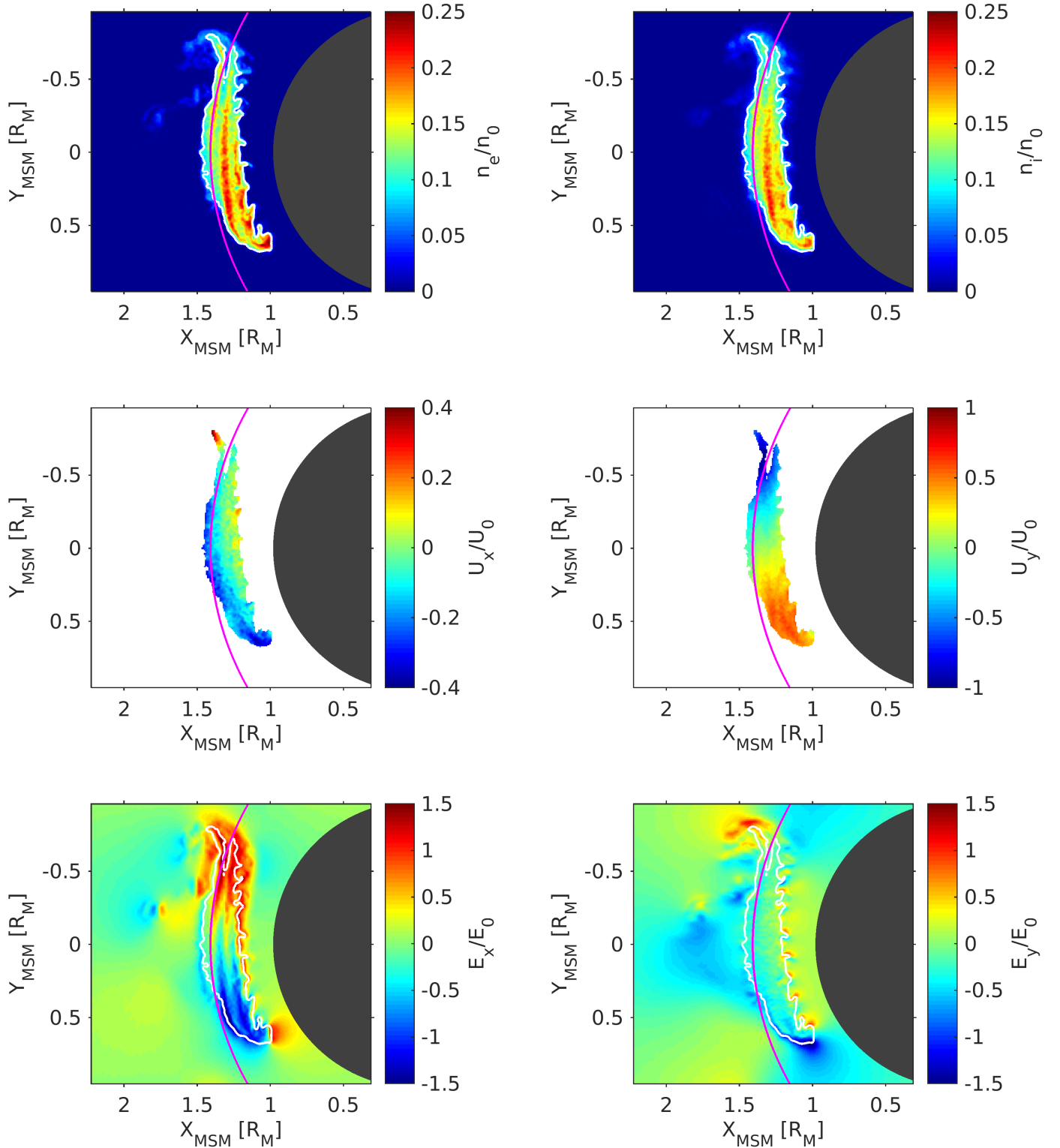


Fig. 4. Cross-section $Z_{\text{MSM}} = 0$ inside the simulation domain for case A: (top) electron and ion number densities, (middle) U_x and U_y components of the plasma bulk velocity, and (bottom) E_x and E_y components of the self-consistent electric field, normalized to their corresponding initial values, at the end of run ($\omega_{\text{Li}}t = 10$). The white contour in the top and bottom panels marks the boundary that separates the higher density bulk of the plasma from its more tenuous regions. The magenta curve is the magnetopause.

The asymmetry is emphasized more clearly in Fig. 6 where we illustrate ion density isosurfaces at the beginning (yellow) and the end of run (purple). The top and middle panels show the 3D simulation box observed from the Sun (top) and from above the north pole (middle). The isosurfaces are drawn for

$n_i/n_0 = 0.33$ at $t = 0$ and $n_i/n_0 = 0.13$ at $\omega_{\text{Li}}t = 10$. While the plasma element or jet is symmetric at injection, its shape changes asymmetrically while moving into the magnetosphere. There is a displacement of the entire plasma element along the $+Y_{\text{MSM}}$ direction. To quantify this asymmetry, we compare the

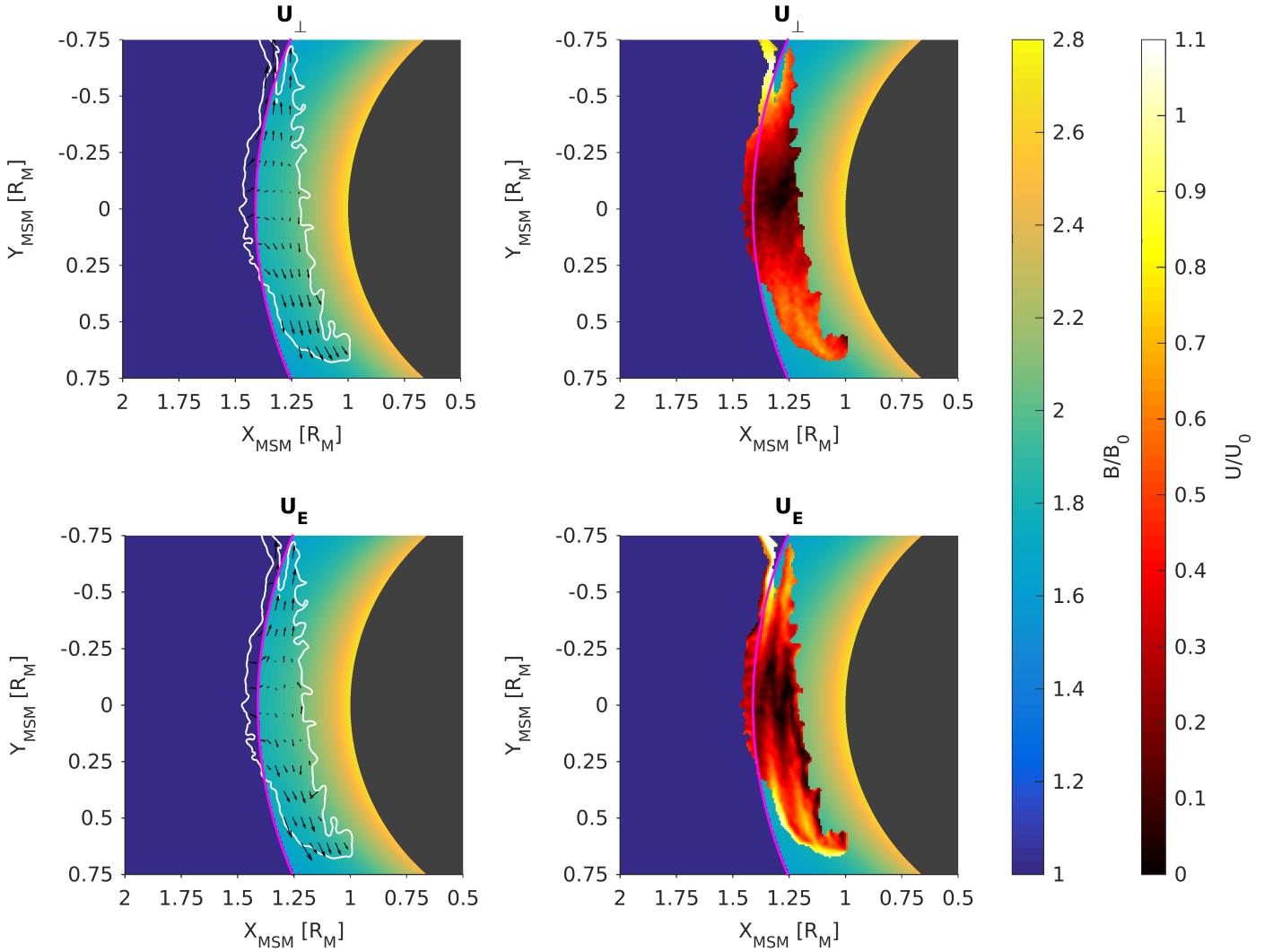


Fig. 5. Perpendicular component of the plasma bulk velocity (top) and the zero-order (or electric) drift velocity (bottom) in the $Z_{\text{MSM}} = 0$ cross-section inside the simulation domain for case A, at the end of run ($\omega_{\perp} t = 10$), illustrated with vectors (left) and color coded (right). The greenish color map shows the magnetic field normalized to its value outside the magnetosphere, while the reddish one the bulk or drift velocity normalized to the injection velocity. The white contour in the left panels encloses the high-density core of the plasma. The magenta curve is the magnetopause.

time evolution of the plasma penetration degree computed for the two magnetospheric flanks: $\Gamma_{\text{MSP}}^{\text{Da}}(t) = M_{\text{IN}}^{\text{Da}}(t)/M_0$ for the dawn flank and $\Gamma_{\text{MSP}}^{\text{Du}}(t) = M_{\text{IN}}^{\text{Du}}(t)/M_0$ for the dusk flank; $M_{\text{IN}}^{\text{Da}}$ is the total mass of plasma penetrating inside the dawn flank of the Hermean magnetosphere (i.e., downstream the magnetopause for $Y_{\text{MSM}} < 0$) at time, t , while $M_{\text{IN}}^{\text{Du}}$ corresponds to the mass of plasma penetrating inside the dusk flank (i.e., downstream the magnetopause for $Y_{\text{MSM}} > 0$). The results obtained are shown in the bottom panel of Fig. 6. While in the early stages of the simulation, we have $\Gamma_{\text{MSP}}^{\text{Da}} \approx \Gamma_{\text{MSP}}^{\text{Du}}$, later on, as the plasma element advances inside the magnetosphere, the penetration degree in the dusk flank exceeds the one in the dawn flank. By the end of run, $\Gamma_{\text{MSP}}^{\text{Da}} = 34\%$ and $\Gamma_{\text{MSP}}^{\text{Du}} = 38\%$. Thus, the amount of solar wind plasma crossing the magnetopause into the dusk flank is larger than the one corresponding to the dawn flank by $(M_{\text{IN}}^{\text{Du}} - M_{\text{IN}}^{\text{Da}})/M_{\text{IN}}^{\text{Da}} = 12\%$.

The impulsive penetration mechanism proposed by Lemaire (1977, 1985) and Lemaire & Roth (1978) embraces a self-consistent kinetic model that couples the first-order guiding center approximation with Ampère's law to explain the entry and transport of solar wind plasma elements inside the

magnetosphere. According to this model, the perpendicular bulk velocity of the finite-sized plasma elements is given by the superposition between the zero-order drift velocity corresponding to the self-polarization electric field and a first-order term corresponding to the gradient-B and curvature drift velocities of the electrons averaged over their corresponding velocity distribution function. The zero-order drift velocity satisfies the following equation for a non-uniform magnetic field (Lemaire 1985):

$$\frac{dU_E}{dt} = -\frac{k(T_{\perp e} + T_{\perp i})}{(m_e + m_i)B} \nabla B - \frac{k(T_{\parallel e} + T_{\parallel i})}{(m_e + m_i)B^2} (\mathbf{B} \cdot \nabla) \mathbf{B}, \quad (2)$$

while the first-order drift velocity, U_1 , is given by (Lemaire 1985):

$$U_1 = -\frac{kT_{\perp e}}{eB^3} \mathbf{B} \times \nabla B - \frac{kT_{\parallel e}}{eB^4} \mathbf{B} \times (\mathbf{B} \cdot \nabla) \mathbf{B}, \quad (3)$$

where $T_{\perp \alpha}$ and $T_{\parallel \alpha}$ are the perpendicular and parallel temperatures of species α with masses m_{α} ; also, k is Boltzmann's constant and e is the elementary charge.

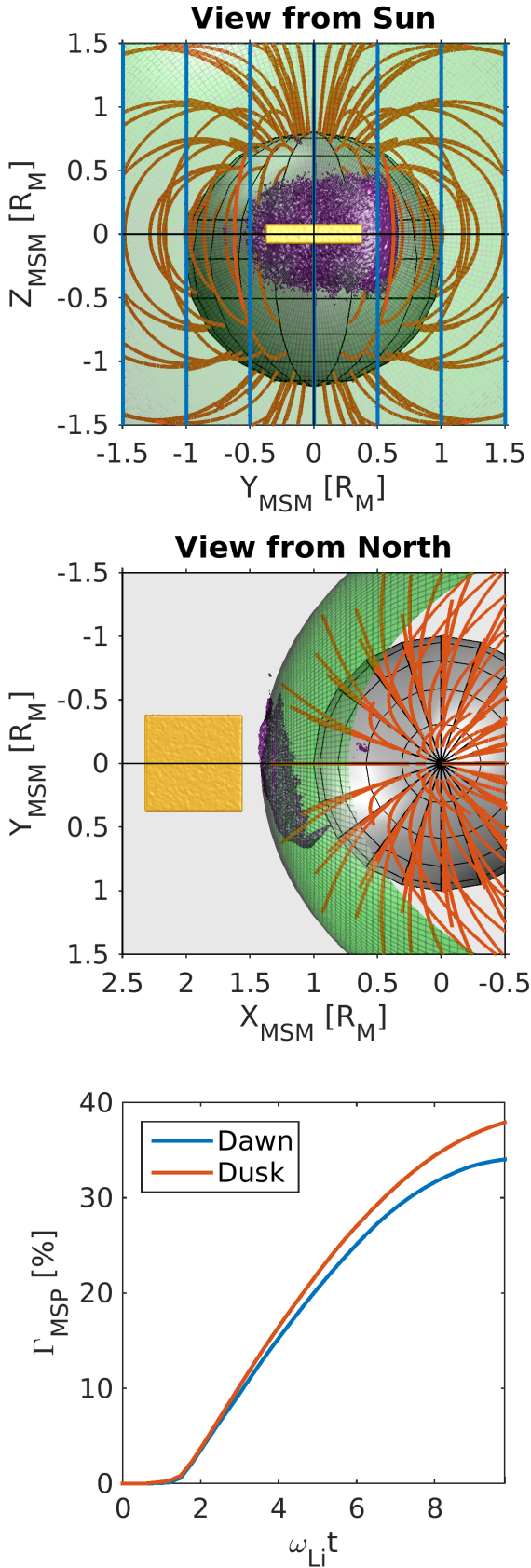


Fig. 6. Views of the simulation domain from the Sun (top) and above the north pole (middle) for case A. We show the ion density isosurface at initialization (yellow) and at the end of run (purple). The magnetospheric penetration degree variation from initialization to the end of run for the dawn (blue curve) and dusk (red curve) flanks (bottom).

We checked if the plasma jet dynamics in our PIC simulations is well described by Eqs. (2) and (3). First, we calculated the zero-order drift velocity that satisfies Eq. (2). For this purpose, we expanded the total time derivative of the zero-order drift velocity in Eq. (2) to obtain a partial differential equation that is further solved with the method of characteristics (e.g., Jeffrey & Dai 2008). The characteristic curves, $\{X(t), Y(t), Z(t)\}$, and the solution of Eq. (2) along them, $\{U_{E,x}(t), U_{E,y}(t), U_{E,z}(t)\}$, are computed numerically for various sets of initial conditions given at $t = 0$. We used central finite-differences to discretize the derivatives in Eq. (2).

The initial velocity distribution functions of the simulated electrons and ions are displaced Maxwellians with equal temperatures: $T_{\perp e0} = T_{\perp i0} = T_{\parallel e0} = T_{\parallel i0} = T_0$. Since the magnetic moment is a constant of motion for both plasma species, the perpendicular temperature increases linearly with the magnetic field magnitude increase: $T_{\perp e} = T_{\perp i} = T_{\perp} = T_0 B/B_0$. On the other hand, for simplicity, we consider the parallel temperature unchanged: $T_{\parallel e} = T_{\parallel i} = T_{\parallel} = T_0$. This constraining condition could be further relaxed to a more general situation with $T_{\parallel} = T_{\parallel}(x, y, z)$, but such an extension is beyond the scope of our current study.

We traced the characteristic curves of Eq. (2) for three different sets of initial conditions that sample the center ($Y_2 = Y_0$) of the plasma element and its lateral edges ($Y_1 = Y_0 - L_{\perp}/2$ and $Y_3 = Y_0 + L_{\perp}/2$) along the $\mathbf{B}_0 \times \mathbf{U}_0$ direction. Thus, we provided the following initialization upstream the magnetopause: $\{X_0, Y_1, Z_0, U_0, 0, 0\}$ for the first curve, $\{X_0, Y_2, Z_0, U_0, 0, 0\}$ for the second curve, and $\{X_0, Y_3, Z_0, U_0, 0, 0\}$ for the third curve. The integration time is $\omega_{\text{Li}} t = 10$. The results obtained are shown in the top panel of Fig. 7. We superposed the three characteristics curves (integrated from $t = 0$ to $\omega_{\text{Li}} t = 10$) onto the PIC solution illustrated in the bottom-left panel of Fig. 5 (at $\omega_{\text{Li}} t = 10$). The characteristic curves are color coded with the magnitude of the zero-order drift velocity that satisfies Eq. (2).

Since the magnetic transition at the simulated magnetopause is very sharp, the guiding center approximation and, consequently, the impulsive penetration model are not valid at the interface between the solar wind and the simulated Hermean magnetosphere. We note that this is just a limitation of this particular simulation and the real thickness of the magnetopause is on the order of several ion Larmor radii (e.g. Roth et al. 1996; Haaland et al. 2004; Dibraccio et al. 2013). In order to surpass this limitation, we considered a supplementary class of initial conditions for the three characteristic curves, provided just downstream the magnetopause. They are extracted from the PIC simulation shortly after the propagation front of the plasma element crosses the magnetopause, namely, at $\omega_{\text{Li}} t = 2$. We note that the PIC solution is independent on the validity of the guiding center approximation. Here, we have the initialization downstream the magnetopause: $\{X'_0, Y_1, Z_0, U'_0, -0.12U_0, 0\}$ for the first curve, $\{X'_0, Y_2, Z_0, U'_0, 0, 0\}$ for the second curve, and $\{X'_0, Y_3, Z_0, U'_0, +0.12U_0, 0\}$ for the third curve, where $X'_0 = 1.36 R_M < R_{\text{ss}}$ and $U'_0 = -0.41U_0$. The integration time covers the interval from $\omega_{\text{Li}} t = 2$ to $\omega_{\text{Li}} t = 10$. The results obtained are shown in the bottom panel of Fig. 7. As expected, the theoretical solution computed for the downstream initialization matches the PIC simulation significantly better than the theoretical solution computed for the upstream initialization. We shall impose a smoother transition of the magnetic field at the magnetopause in our future simulations.

It can be easily noticed that the two lateral characteristic curves are deflected symmetrically inside the magnetospheric

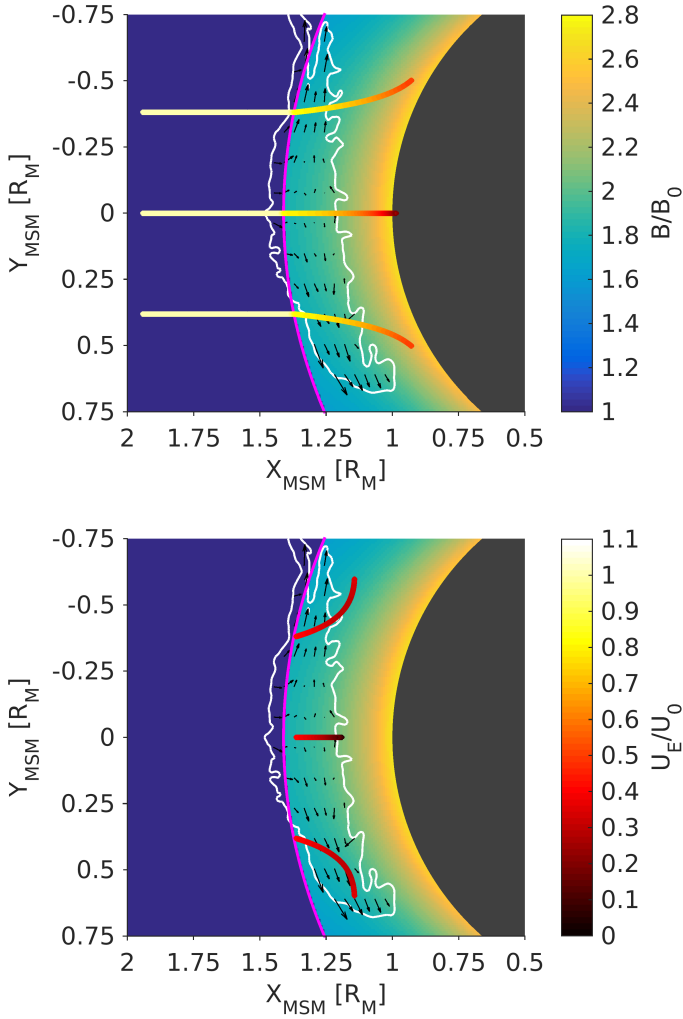


Fig. 7. Three characteristic curves of Eq. (2) traced in the equatorial plane ($Z_{\text{MSM}} = 0$). The initial conditions correspond to the central region of the plasma element and its lateral edges. The curves are color coded with the magnitude of the zero-order drift velocity that satisfies Eq. (2) and superposed onto the PIC solution illustrated in the bottom-left panel of Fig. 5. The characteristic curves are computed for two different classes of initial conditions: upstream (top) and downstream (bottom) the magnetopause.

cavity, while the central one remains unperturbed. Indeed, the curve initialized in $Y_1 < 0$ is pushed downward, while the one initialized in $Y_3 > 0$ is pushed duskward. On the other hand, the zero-order drift velocity is significantly reduced for larger values of the magnetic field. For the central characteristic curve initialized in $Y_2 = 0$, the zero-order drift velocity at $\omega_{\text{Li}}t = 10$ is $U_{\text{E},x} = -0.20 U_0$ for the upstream initialization and $U_{\text{E},x} = +0.16 U_0$ for the downstream initialization. Thus, the forward motion is strongly slowed down and even stopped and reversed towards the $+X_{\text{MSM}}$ axis. This behavior is also observed in our PIC simulations. Indeed, the bulk velocity at the propagation front of the plasma element near the equatorial plane is slightly positive, $U_x \approx +0.10 U_0$, as can be seen in Figs. 3 and 4.

The dominant symmetrical deflection of the plasma element in the equatorial plane is generated through the zero-order drift velocity. However, the PIC simulations also show a displacement of the entire plasma structure along the $+Y_{\text{MSM}}$ direction. To address this behavior, we investigated the first-order drift velocity given by Eq. (3). Using the assumptions on the temperature

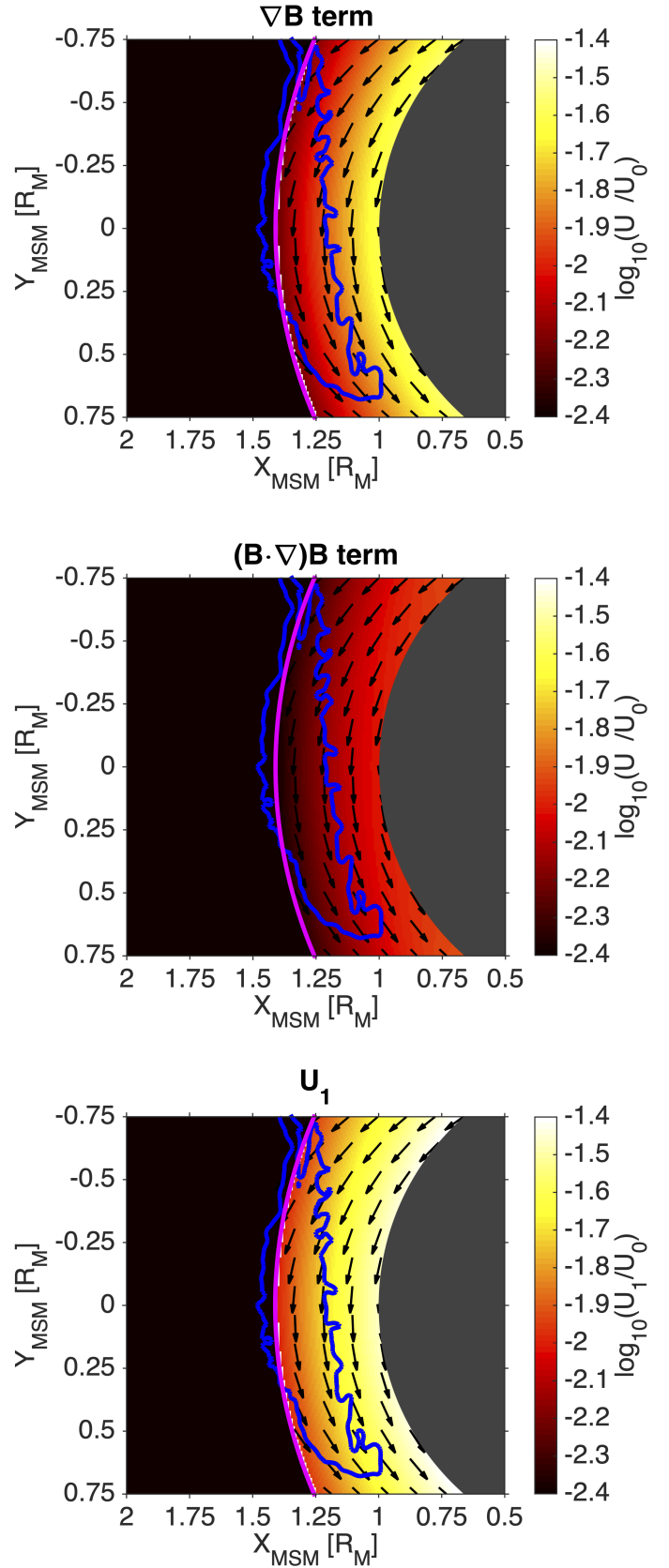


Fig. 8. First-order drift velocity given by Eq. (3) in the equatorial plane ($Z_{\text{MSM}} = 0$): (top) gradient-B term, (middle) curvature term, and (bottom) sum of both terms. The orientation of the velocity field is illustrated with unit vectors, while the magnitude is color-coded. The blue contour encloses the high-density core of the simulated plasma element. The magenta curve is the magnetopause.

variation considered for solving Eq. (2), we computed the spatial distribution of U_1 . The results obtained are shown in Fig. 8 for the total first-order drift velocity field and its gradient-B and curvature terms.

We can notice that the U_{1x} component of the first-order drift velocity is positive in the dawn flank and negative in the dusk flank. On the other hand, the U_{1y} component is always positive. The magnitude, U_1 , increases as we advance inside the magnetosphere and is larger in the front than in the flanks (for a fixed X_{MSM} value). At the propagation front of the simulated plasma element, we have $U_1 = 0.02 U_0$ in $Y_{\text{MSM}} = 0$ and $U_1 = 0.025 U_0$ in $Y_{\text{MSM}} = 0.63 R_M$. With respect to the local value of the plasma bulk velocity, $U_1 \approx 0.50 U_\perp$ around $Y_{\text{MSM}} = 0$ and decreases to $U_1 \approx 0.05 U_\perp$ around $Y_{\text{MSM}} = 0.63 R_M$. The ratio between the gradient-B and curvature terms in Eq. (3) is $U_1^{\nabla B}/U_1^{crv} \in [-1.2, \sim 2.6]$, with an average value of ~ 1.8 . This ratio decreases for larger parallel temperatures.

Figure 9 shows the variation of $|Y(t)|$ for the two lateral characteristic curves initialized in the dawn ($|Y_{\text{Da}}(t)|$, solid lines) and dusk ($|Y_{\text{Du}}(t)|$, dashed lines) flanks of the magnetosphere. The top and bottom panels correspond to the theoretical solution computed for the upstream and downstream initial conditions, respectively. The total time derivative of U_E in Eq. (2) is expanded by considering the following two approaches: (i) with $V = U_E$ (blue lines), as in Fig. 7, and (ii) with $V = U_E + U_1$ (red lines), where $V = (dX/dt, dY/dt, dZ/dt)$. In this way, we can directly estimate the quantitative impact of the first-order drift velocity on the dawn-dusk deflection of plasma. As can be noticed in both panels of Fig. 9, the $\pm Y_{\text{MSM}}$ displacement of the two characteristic curves is symmetrical ($\Delta|Y(t)| = |Y_{\text{Du}}(t)| - |Y_{\text{Da}}(t)| = 0$) when we neglect the first-order term given by Eq. (3). On the other hand, the $\pm Y_{\text{MSM}}$ displacement is clearly asymmetric when the first-order drift velocity is included in the theoretical solution. Indeed, $\Delta|Y|$ increases inside the magnetosphere up to $0.09 R_M$ for the upstream initialization and $0.03 R_M$ for the downstream initialization. The duskward (dawnward) advance of the dusk (dawn) curve is larger (smaller) than the one corresponding to the symmetrical displacement, leading to the dawn-dusk asymmetric evolution of the plasma element streaming inside the magnetosphere.

The first-order drift velocity given by Eq. (3) is characterized by a dawn-dusk component in both magnetospheric flanks. This first-order term pushes the plasma towards the positive Y_{MSM} axis and further leads to an enhanced accumulation of particles in the dusk flank, as shown in Fig. 6. It also generates the asymmetry observed in the X_{MSM} component of the plasma bulk velocity illustrated in Fig. 4. Indeed, while $U_{E,x} < 0$ in both flanks, the distribution of U_{1x} is antiparallel ($U_{1x} \geq 0$ for $Y_{\text{MSM}} \leq 0$) and, consequently, enlarges the antisunward component of the plasma bulk velocity in the dusk flank with respect to the dawn flank, leading to the observed asymmetry. To better emphasize this effect, we performed two supplemental simulations with plasma elements injected from the two magnetospheric flanks.

The results obtained are shown in Fig. 10 for both cases B (dawn flank injection – blue box in Fig. 1) and C (dusk flank injection – purple box in Fig. 1). The minimum distance between the initial propagation front of the plasma elements and the local magnetopause surface is identical to the one used in case A, namely, $\Delta R = 2.6 r_{Li} = 0.15 R_M$. At the local magnetopause, in $Y_{\text{MSM}} = \pm 0.76 R_M$, the background magnetic field increases by 62% with respect to the solar wind value. The simulation is stopped at $\omega_{Li}t = 11$ when the planetary penetration degree is still small, namely, 4% in case B and 3% in case C.

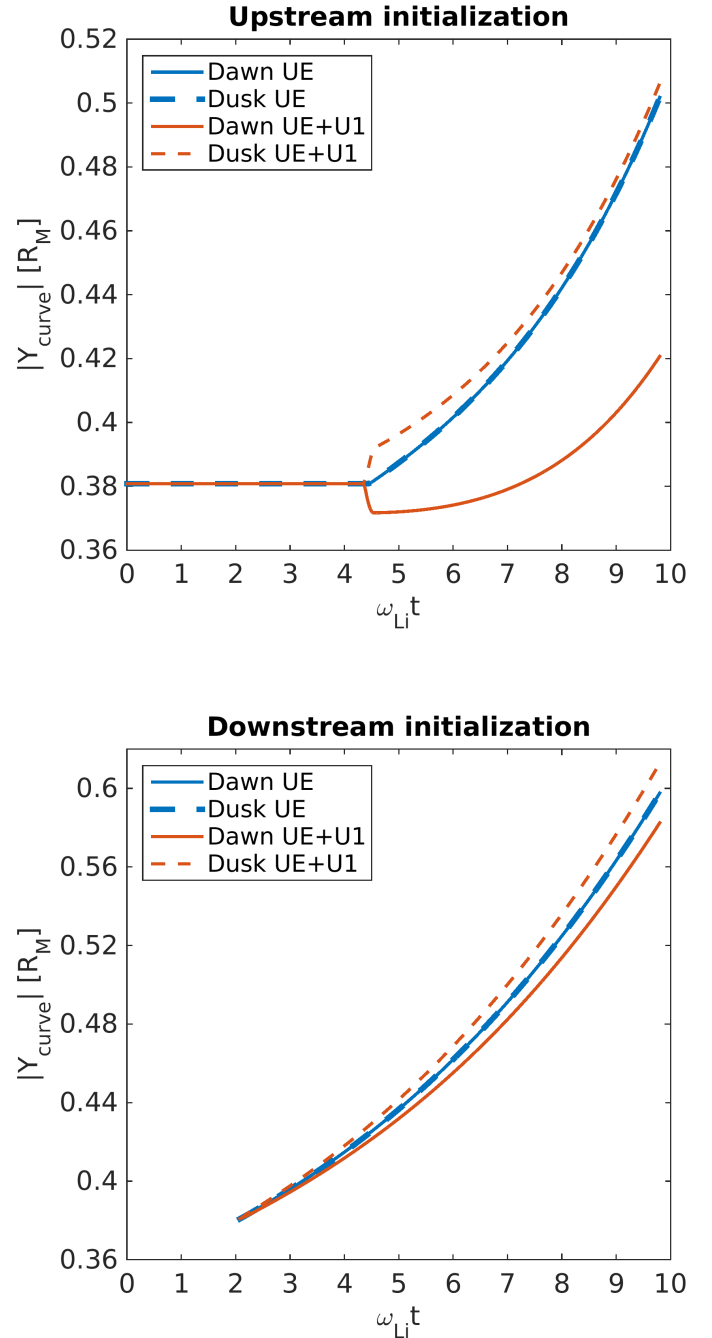


Fig. 9. Time evolution of the Y_{MSM} coordinate for the two lateral characteristic curves illustrated in Fig. 7: upstream initialization (top) and downstream initialization (bottom). The characteristic curves are calculated with $V = U_E$ (blue lines) and $V = U_E + U_1$ (red lines).

We illustrate in Fig. 10 the electron number density (left panels) and the perpendicular plasma bulk velocity (right panels) in the cross-section $Z_{\text{MSM}} = 0$. Various dynamical properties of the two plasma elements are listed in Table 2. The equatorial evolution of the two simulated plasmas is different, as can be seen in both density and velocity color maps of Fig. 10. Indeed, the dusk flank injection is accompanied by a deeper penetration, while the dawn flank injection is less efficient. The total magnetospheric penetration degree at the end of run ($\omega_{Li}t = 11$) is 60% in case B and 70% in case C. Thus, the amount of plasma crossing the magnetopause surface is 17% larger in the dusk flank with respect to the dawn flank. On the other hand, as in case A, the

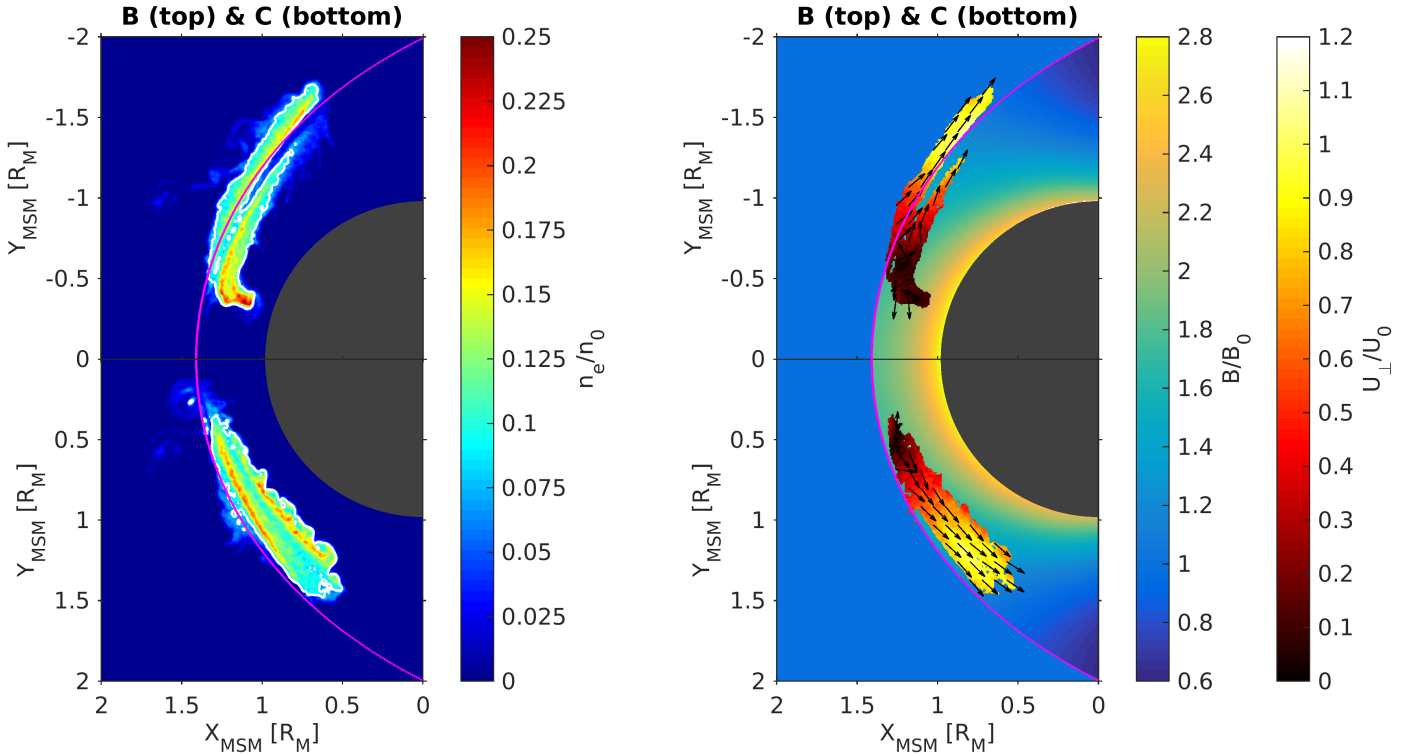


Fig. 10. Cross-section $Z_{\text{MSM}} = 0$ inside the simulation domain for cases B (top) and C (bottom) at $\omega_{\text{Li}} t = 11$: electron number density (left) and perpendicular plasma bulk velocity (right: reddish color map and black unit vectors) superposed onto the background magnetic field magnitude (right: greenish color map). All quantities are normalized to their corresponding initial values.

Table 2. Magnetospheric penetration and dynamical properties

Parameter	Case B	Case C
$\Gamma_{\text{MSP}} [\%]$	60	70
$X_{\text{F}} [R_{\text{M}}]$	0.89	0.63
$U_{\text{x}}^{\text{F}}/U_0$	-0.37	-0.72
U_{\perp}^{F}/U_0	0.78	0.89
U_{\perp}^{T}/U_0	0.09	0.02
U_1^{F}/U_0	0.017	0.024
U_1^{T}/U_0	0.015	0.015
$U_1^{\text{F}}/U_{\perp}^{\text{F}}$	0.022	0.027
$U_1^{\text{T}}/U_{\perp}^{\text{T}}$	0.17	0.75

Notes. Data provided for the plasma elements simulated in cases B (dawn flank injection) and C (dusk flank injection) at the end of run ($\omega_{\text{Li}} t = 11$). Γ_{MSP} – penetration degree inside the magnetosphere, X_{F} – position of the propagation front along the X_{MSM} axis, R_{M} – radius of planet Mercury, $U_{\text{x}}^{\text{F}} - U_{\text{x}}$ component of the plasma bulk velocity at the propagation front, U_{\perp}^{F} and U_{\perp}^{T} – perpendicular plasma bulk velocity at the propagation front and trailing edge, U_1^{F} and U_1^{T} – first-order drift velocity at the propagation front and trailing edge, U_0 – plasma bulk velocity at injection. Except for Γ_{MSP} , all other quantities are computed in the equatorial plane ($Z_{\text{MSM}} = 0$).

magnetospheric entry is accompanied by the braking of plasma while streaming into the larger magnetic field. The deceleration is different in the two cases. The perpendicular bulk velocity at the propagation front of the plasma element is 14% larger for the dusk flank injection, where $U_{\perp} = 0.89 U_0$. On the other hand,

at the trailing edge, $U_{\perp} \approx 0$ in both cases. The U_{x}^{F} component of the bulk velocity at the propagation front is almost two times larger for the dusk flank injection, leading to a deeper penetration of plasma inside the magnetosphere, down to $0.63 R_{\text{M}}$ in case C versus $0.89 R_{\text{M}}$ in case B. The magnitude of the first-order drift velocity with respect to the local value of the total plasma bulk velocity varies from 2% (at the propagation front) to 75% (at the trailing edge), as listed in Table 2. Thus, the penetrating plasma is pushed and braked asymmetrically inside the magnetosphere along the Y_{MSM} axis by first-order drift effects.

4. Conclusions

In the present paper, we use 3D PIC simulations to investigate the interaction between solar wind or magnetosheath plasma elements (or irregularities, jets) and the dayside Hermean magnetosphere. The finite-sized jets are streaming towards the magnetopause of Mercury for a northward orientation of the interplanetary magnetic field. We focus on the interaction of the plasma elements with the non-uniform magnetospheric field of planet Mercury and disregard the effects of the background plasma. Here are the main findings of our work:

1. The solar wind plasma elements are able to cross the magnetopause and penetrate inside the Hermean magnetosphere. The jets' entry is accompanied by strong braking while streaming into the increasingly larger magnetic field. By reducing the height of the magnetic barrier, the amount of solar wind plasma crossing the magnetopause surface increases.
2. The plasma elements are deflected in the equatorial plane along both positive and negative directions of the Y_{MSM} axis as they enter inside the magnetosphere. The equatorial

deflection is asymmetrical. The amount of solar wind plasma crossing the magnetopause surface into the dusk flank is larger than the one corresponding to the dawn flank. Conversely, the braking of the plasma elements is stronger in the dawn flank. Thus, the solar wind plasma elements interacting with the dusk flank magnetopause are able to penetrate deeper inside the Hermean magnetosphere.

3. The plasma dynamics revealed by our PIC simulations is consistent with the impulsive penetration mechanism. The self-polarization electric field acting inside the quasineutral bulk of plasma sustains the motion across the transverse magnetic field and further determines its equatorial deflection along the Y_{MSM} axis. Although it is symmetrical in the zero-order approximation, the equatorial dynamics is characterized by a dawn-dusk asymmetry generated through first-order drift effects. The duskward deflection of the solar wind plasmoids penetrating impulsively in the magnetosphere has been advocated for the first time by Lemaire (1985) for the terrestrial magnetosphere. This study stands as the first numerical confirmation of this kinetic effect.

The physical mechanism we discuss in this paper can explain the transport of high-speed plasma jets across the frontside magnetopause of the planet Mercury in the context of the northward IMF. The BepiColombo mission provides a great opportunity to search for such kinds of plasma structures using in situ data in the vicinity of the Hermean magnetopause.

Acknowledgements. The authors acknowledge support from the Romanian Ministry of Research, Innovation and Digitalization through projects PN-III-P1-1.1-TE-2019-1288 (SMART), PN-III-P1-1.1-TE-2021-0102 (TWISTER) and National Core Program LAPLAS VII (30N/2023) and also from the European Space Agency through PRODEX project PEA 4000134960 (MISSION). Marius Echim acknowledges support from the Belgian Solar-Terrestrial Centre of Excellence (STCE) in Brussels, Belgium.

References

- Amata, E., Savin, S. P., Ambrosino, D., et al. 2011, *Planet. Space Sci.*, **59**, 482
- Anderson, B. J., Johnson, C. L., & Korth, H. 2013, *Geochem. Geophys. Geosyst.*, **14**, 3875
- Archer, M. O., & Horbury, T. S. 2013, *Ann. Geophys.*, **31**, 319
- Borovsky, J. E. 1987, *Phys. Fluids*, **30**, 2518
- Buneman, O. 1993, in *Computer Space Plasma Physics: Simulation Techniques and Software*, eds. H. Matsumoto, & Y. Omura (Tokyo: Terra Scientific Company)
- Cai, D. S., & Buneman, O. 1992, *Phys. Fluids B*, **4**, 1033
- Chen, F. F. 1984, *Introduction to Plasma Physics and Controlled Fusion*, 2nd edn., Vol. 1: Plasma Physics (New York: Plenum Press)
- Dai, W., & Woodward, P. R. 1994, *J. Geophys. Res.*, **99**, 8577
- Dai, W., & Woodward, P. R. 1995, *J. Geophys. Res.*, **100**, 14843
- Dai, W., & Woodward, P. R. 1998, *J. Plasma Phys.*, **60**, 711
- Dibraccio, G. A., Slavin, J. A., Boardsen, S. A., et al. 2013, *J. Geophys. Res. (Space Phys.)*, **118**, 997
- Dmitriev, A. V., & Suvorova, A. V. 2015, *J. Geophys. Res. (Space Phys.)*, **120**, 4423
- Dmitriev, A. V., Lalchand, B., & Ghosh, S. 2021, *Universe*, **7**, 152
- Echim, M. M., & Lemaire, J. F. 2000, *Space Sci. Rev.*, **92**, 565
- Echim, M. M., & Lemaire, J. F. 2005, *Phys. Rev. E*, **72**, 036405
- Escoubet, C. P., Hwang, K. J., Toledo-Redondo, S., et al. 2020, *Front. Astron. Space Sci.*, **6**, 78
- Fatemi, S., Poppe, A. R., Delory, G. T., & Farrell, W. M. 2017, in *Journal of Physics Conference Series*, **837**, 012017
- Fatemi, S., Poppe, A. R., & Barabash, S. 2020, *J. Geophys. Res. (Space Phys.)*, **125**, e27706
- Galvez, M. 1987, *Phys. Fluids*, **30**, 2729
- Galvez, M., & Borovsky, J. E. 1991, *Phys. Fluids B*, **3**, 1892
- Galvez, M., Gary, S. P., Barnes, C., & Winske, D. 1988, *Phys. Fluids*, **31**, 1554
- Goncharov, O., Gunell, H., Hamrin, M., & Chong, S. 2020, *J. Geophys. Res. (Space Phys.)*, **125**, e27667
- Gunell, H., Hurlig, T., Nilsson, H., Koepke, M., & Brenning, N. 2008, *Plasma Phys. Controlled Fusion*, **50**, 074013
- Gunell, H., Walker, J. J., Koepke, M. E., et al. 2009, *Phys. Plasmas*, **16**, 112901
- Gunell, H., Nilsson, H., Stenberg, G., et al. 2012, *Phys. Plasmas*, **19**, 072906
- Gunell, H., Stenberg Wieser, G., Mella, M., et al. 2014, *Ann. Geophys.*, **32**, 991
- Haaland, S., Sonnerup, B., Dunlop, M., et al. 2004, *Ann. Geophys.*, **22**, 1347
- Huba, J. D. 1996, *J. Geophys. Res.*, **101**, 24855
- Hurlig, T., Brenning, N., & Raadu, M. A. 2003, *Phys. Plasmas*, **10**, 4291
- Hurlig, T., Brenning, N., & Raadu, M. A. 2004, *Phys. Plasmas*, **11**, L33
- Jeffrey, A., & Dai, H.-H. 2008, *Handbook of Mathematical Formulas and Integrals*, 4th edn. (USA: Academic Press)
- Karimabadi, H., Roytershteyn, V., Vu, H. X., et al. 2014, *Phys. Plasmas*, **21**, 062308
- Karlsson, T., Brenning, N., Nilsson, H., et al. 2012, *J. Geophys. Res. (Space Phys.)*, **117**, A03227
- Karlsson, T., Kullen, A., Liljeblad, E., et al. 2015, *J. Geophys. Res. (Space Phys.)*, **120**, 7390
- Karlsson, T., Liljeblad, E., Kullen, A., et al. 2016, *Planet. Space Sci.*, **129**, 61
- Karlsson, T., Heyner, D., Volwerk, M., et al. 2021, *J. Geophys. Res. (Space Phys.)*, **126**, e28961
- Korth, H., Johnson, C. L., Philpott, L., Tsyganenko, N. A., & Anderson, B. J. 2017, *Geophys. Res. Lett.*, **44**, 10,147
- Lavorenti, F., Henri, P., Califano, F., et al. 2022, *A&A*, **664**, A133
- Lemaire, J. 1977, *Planet. Space Sci.*, **25**, 887
- Lemaire, J. 1985, *J. Plasma Phys.*, **33**, 425
- Lemaire, J., & Roth, M. 1978, *J. Atmos. Terrestrial Phys.*, **40**, 331
- Livesey, W. A., & Pritchett, P. L. 1989, *Phys. Fluids B*, **1**, 914
- Lundin, R., & Aparicio, B. 1982, *Planet. Space Sci.*, **30**, 81
- Lundin, R., Sauvaud, J. A., Rème, H., et al. 2003, *Ann. Geophys.*, **21**, 457
- Lyatsky, W., Pollock, C., Goldstein, M. L., Lyatskaya, S., & Avakov, L. 2016a, *J. Geophys. Res. (Space Phys.)*, **121**, 7699
- Lyatsky, W., Pollock, C., Goldstein, M. L., Lyatskaya, S., & Avakov, L. 2016b, *J. Geophys. Res. (Space Phys.)*, **121**, 7713
- Ma, Z. W., Hawkins, J. G., & Lee, L. C. 1991, *J. Geophys. Res.*, **96**, 15751
- Markidis, S., Lapenta, G., & Rizwan-uddin. 2010, *Math. Comput. Simul.*, **80**, 1509
- Neubert, T., Miller, R. H., Buneman, O., & Nishikawa, K. I. 1992, *J. Geophys. Res.*, **97**, 12057
- Němeček, Z., Šafránková, J., Přeč, L., et al. 1998, *Geophys. Res. Lett.*, **25**, 1273
- Palmroth, M., Hietala, H., Plaschke, F., et al. 2018, *Ann. Geophys.*, **36**, 1171
- Palmroth, M., Raptis, S., Suni, J., et al. 2021, *Ann. Geophys.*, **39**, 289
- Plaschke, F., Hietala, H., & Angelopoulos, V. 2013, *Ann. Geophys.*, **31**, 1877
- Plaschke, F., Hietala, H., Angelopoulos, V., & Nakamura, R. 2016, *J. Geophys. Res. (Space Phys.)*, **121**, 3240
- Preisser, L., Blanco-Cano, X., Kajdič, P., Burgess, D., & Trotta, D. 2020, *ApJ*, **900**, L6
- Raptis, S., Karlsson, T., Plaschke, F., Kullen, A., & Lindqvist, P.-A. 2020, *J. Geophys. Res. (Space Phys.)*, **125**, e27754
- Roth, M., De Keyser, J., & Kuznetsova, M. M. 1996, *Space Sci. Rev.*, **76**, 251
- Savin, S., Amata, E., Zelenyi, L., et al. 2012, *Ann. Geophys.*, **30**, 1
- Savoini, P., Scholer, M., & Fujimoto, M. 1994, *J. Geophys. Res.*, **99**, 19377
- Schmidt, G. 1960, *Phys. Fluids*, **3**, 961
- Shi, Q. Q., Zong, Q. G., Fu, S. Y., et al. 2013, *Nat. Commun.*, **4**, 1466
- Shue, J. H., Chao, J. K., Fu, H. C., et al. 1997, *J. Geophys. Res.*, **102**, 9497
- Voitcu, G., & Echim, M. 2016, *J. Geophys. Res. (Space Phys.)*, **121**, 4343
- Voitcu, G., & Echim, M. 2017, *Geophys. Res. Lett.*, **44**, 5920
- Voitcu, G., & Echim, M. 2018, *Ann. Geophys.*, **36**, 1521
- Vuorinen, L., Hietala, H., & Plaschke, F. 2019, *Ann. Geophys.*, **37**, 689
- Wessel, F. J., Hong, R., Song, J., et al. 1988, *Phys. Fluids*, **31**, 3778
- Wing, S., Johnson, J. R., Chaston, C. C., et al. 2014, *Space Sci. Rev.*, **184**, 33